Construction and Building Materials 229 (2019) 116543

Contents lists available at ScienceDirect

Construction and Building Materials

journal homepage: www.elsevier.com/locate/conbuildmat

# Hygro-mechanical modeling of restrained ring test: COST TU1404 benchmark

Vít Šmilauer [a,*], Petr Havlásek [a], Tobias Gasch [b], Arnaud Delaplace [c], David E.-M. Bouhjiti [d], Farid Benboudjema [e], Matthieu Briffaut [f], Fragkoulis Kanavaris [g,1], Miguel Azenha [h]

[a] Czech Technical University in Prague, Faculty of Civil Engineering, Department of Mechanics, Thákurova 7, 166 29 Prague 6, Czech Republic
[b] KTH Royal Institute of Technology, Brinellvägen 23, Stockholm, 11428, Sweden
[c] LafargeHolcim Research Center, Isle d'Abeau, 38070, France
[d] Grenoble INP Partnership Foundation (Industrial chair PERENITI) – Univ. Grenoble Alpes, CNRS, Grenoble INP, 3SR, F-38000, France
[e] ENS Paris-Saclay (ENS Cachan), 94230 Cachan, France
[f] Université Grenoble Alpes, CNRS, Grenoble INP, 3SR, 38000 Grenoble, France
[g] Currently in Specialist Technology and Research, ADE, Arup, London, W1T 4BQ, UK
[h] ISISE, University of Minho, Guimarães, 4800-058, Portugal

## HIGHLIGHTS

- Six teams simulated ring shrinkage test using different hygro-mechanical models.
- Experimental data for desorption isotherm, E modulus, strength evolution, basic creep.
- Validated mass loss and axial deformation of a prism, hoop strain in the ring.
- Interface effect between concrete and steel explored.
- Negligible role of concrete notch.

## ARTICLE INFO

*Article history:*
Received 14 March 2019
Received in revised form 19 June 2019
Accepted 20 July 2019

*Keywords:*
Restrained ring test
Hygro-mechanical simulation
Moisture
Transport
Shrinkage
Creep
Crack

## ABSTRACT

The restrained ring test belongs to a traditional method for estimating cracking tendency of a paste, mortar or concrete mix. The test involves hygro-mechanical interactions with intricate interplay of several phenomena, such as autogenous shrinkage, drying shrinkage, basic and drying creep, together with evolution of tensile strength and fracture energy. The benchmark described in this paper relies on extensive experimental data sets obtained through the extended Round Robin Testing programme (RRT+) of COST Action TU1404. Six teams took part with their simulation models. A series of outputs were produced, starting from mass loss of a prism through its axial deformation up to hoop stress/strain evolution in the ring. Four teams quantified also damage due to drying and strain concentrations. All models showed excellent performance on mass loss while strain validation showed higher scatter and influence of several factors. The benchmark demonstrated high capability of used models and emphasized strong role of calibration with regards to available experimental data.



## 1. Introduction

Restrained ring test is a well-established method for testing cementitious binders for cracking tendency during early ages, documented historically on at least 13 different ring dimensions [1] and now adopted in several standards such as ASTM C1581 or AASHTO T334. The test is driven by tensile stresses induced by restrained chemical/autogenous and drying shrinkage which are resisted to an extent by the material's tensile strength and are also partially relaxed due to viscoelasticity. The ring tests usually have

* Corresponding author.
*E-mail addresses:* vit.smilauer@fsv.cvut.cz (V. Šmilauer), petr.havlasek@fsv.cvut.cz (P. Havlásek), tobias.gasch@byv.kth.se (T. Gasch), arnaud.delaplace@lafargeholcim.com (A. Delaplace), david.bouhjiti@3sr-grenoble.fr (D.E.-M. Bouhjiti), farid.benboudjema@ens-paris-saclay.fr (F. Benboudjema), matthieu.briffaut@3sr-grenoble.fr (M. Briffaut), frag.kanavaris@arup.com (F. Kanavaris), miguel.azenha@civil.uminho.pt (M. Azenha).

[1] Previously in ISISE, University of Minho, Guimarães, 4800-058, Portugal.

https://doi.org/10.1016/j.conbuildmat.2019.07.269
0950-0618/

very low thermal gradients and thermal cracking plays no significant role [2].

Several concrete structures, such as slabs or pavements, may exhibit cracking due to the combination of the aforementioned phenomena. Historically, the first documented ring tests were conducted by R. Carlson already in 1939–1942 [3], followed by many researchers such as Blaine, Krauss and Rogalla [4], Weiss and Shah [5], Wang et al. [6] or Turcry et al. [7]; an in-depth review on this subjected has already been provided by Kanavaris et al. [8].

The short-time restrained ring test provided a strong correlation with long-term concrete cracking [3]; such experiment was conducted on 28 various cements used for 104 panels of size $2.74 \times 1.22 \times 0.41$ m placed in 1943 around Green Mountain Dam, Colorado. Cracking time of the ring correlated well with concrete surface cracking after 53 years; the sooner the ring cracked, the more severe cracking appeared later [3]. Low alkali cements, coarser cements and lower $C_3A$ cement performed the best. Heat of hydration was not an issue.

Prolonging ring's cracking time can generally happen by lowering autogeneous and drying shrinkage, increasing concrete creep while maintaining sufficient tensile strength gain. Common methods include decreasing binder content, decreasing alkali content, using cements with slower hydration kinetics, or decelerating drying kinetics. Furthermore, the geometrical characteristics of the steel and concrete rings, which directly affect the degree of restraint in the system, can be adjusted so that stress generation and testing time are optimised [3,9–11]. A study on the ring test dimensions showed that a thinner steel ring led to prolonged cracking time due to less external restraint and that larger drying surface led to shorter cracking time [12].

Rings drying from top and bottom lead to non-uniform hoop stress across the height of the concrete ring's cross section. Analytical formulas in elastic and viscoelastic domains have been proposed, averaging hoop stress over the concrete height [12,13]. Role of moisture gradient, concrete thickness and restraining effect were studied using hygro-mechanical simulations [14]. Numerical approach was found to bring more accurate stress/strain fields by introducing fracture mechanics, viscoelastic behavior depending on local moisture conditions, interfaces, boundary conditions, or circular/elliptical ring geometries [15,16].

This benchmark aims at validating ring test behavior with more accurate numerical models which should bring deeper insight in mechanisms occurring during restrained ring shrinkage, i.e. interplay of drying, creep, shrinkage and crack propagation using linked/staggered multiphysical simulations.

### 1.1. COST TU1404 action

COST Action TU1404 "Towards the next generation of standards for service life of cement-based materials and structures" has set up benchmark "GP2.c-Macro modeling-Ring test" to validate experimental results on a reference concrete (labelled as 'OC') and to test different modelling approaches. Concrete mix design mimicked concrete used in older nuclear French containments [17] with rather lower amount of binder, finer cement, lower alkali content and low autogeneous shrinkage.

Fig. 1 shows the ring's geometry with sealed outer surface used in the benchmark, drying from top and bottom surfaces. The inner steel ring was 25 mm thick, providing high external restraint to the concrete.

Interested participants received input experimental data in advance in order to calibrate their models, specifically:

- Concrete and cement compositions.
- Released heat from isothermal calorimetry.
- Desorption isotherm for mature concrete.

**Fig. 1.** Setup of the ring test (Courtesy of E. Roziére) [18].

- Evolution of E modulus, splitting tensile and compressive strength.
- Basic creep for load applied at 1 and 3 days.
- Autogenous shrinkage.
- Total shrinkage and mass loss on prism $100 \times 100 \times 400$ mm.
- Evolution of hoop strain evolution on the inner surface of the steel ring.

The participants were free to use their modelling approaches and models, however, several intermediate steps were required to validate their results. Six teams took part in the benchmark, namely

| | |
|---|---|
| Team 1 | Arup (UK) + University of Minho (Portugal) |
| Team 2 | CTU in Prague (Czech Republic) |
| Team 3 | KTH Royal Institute of Technology, Stockholm (Sweden) |
| Team 4 | LafargeHolcim Research Center, Isle d'Abeau (France) |
| Team 5 | Industrial chair PERENITI – 3SR Lab, Grenoble (France) |
| Team 6 | ENS Paris-Saclay (ENS Cachan) and Université Grenoble Alpes (France) |

Supplementary XLSX data file is provided at the journal's data repository with data provided to participants prior to the benchmark.

## 2. Material and experimental data

Experiments with their details were defined in Extended Round Robin testing programme (RRT+) of COST TU1404 [19]. The concrete mix considered was an ordinary medium-strength concrete with $w_{eff}/c = 0.52$[19] whilst its composition (see Table 1) was

**Table 1**
Concrete composition.

| Component | Type of the material | Amount ($kg \cdot m^{-3}$) |
|---|---|---|
| Cement | CEM I 52.5N-SR3 CE PM-CP2 NF HRC Gaurain, Blaine 440 $m^2/kg$, $Na_2O$ eq. 0.48 % | 320 |
| Dry sand | 0–4 mm, REC GSM LGP1 (13 % CaO and 72 % $SiO_2$) | 830 |
| Fully saturated gravel | 4–11 mm, R GSM LGP1 (rounded, containing silicate and limestone) | 449 |
| | 8–16 mm, R Balloy (rounded, containing silicate and limestone) | 564 |
| Admixtures | Plasticizer SIKAPLAST Techno 80 | 1.44 |
| Added water | Water added to the mixer | 172.4 |

very much similar to that of the concrete used in the VeRCoRs project [17].

The evolution of compressive strength originated from cylinders ø100 × 200–ø150 × 300 mm while splitting tensile strength was measured on cylinders ø80 × 300–ø150 × 300 mm, see Fig. 2. The teams used analytical approximations to assess tensile strength for crack initiation.

Isothermal calorimetry at 20°C characterized hydration kinetics of cement paste, see Fig. 3. Theoretical heat of hydration is estimated as 510 J/g from mineral composition. Degree of hydration served only for Team 3 during estimation of water consumption. Team 1 also utilized the hydration heat results to calculate the thermal behaviour of the concrete ring only to compute near-negligible temperature gradients at early ages.

Autogenous shrinkage was measured from 1 up to 64 days of hydration, see Fig. 4. Extrapolation up to 2000 days used B4 model formula for autogeneous shrinkage, scaled by a factor of 0.59 to match short-term data [20]. At the age of 2000 days, autogeneous shrinkage reached 43 $\mu\varepsilon$. Accompanying measurements at another lab yielded higher shrinkage 75 $\mu\varepsilon$ at 22 days, however, due to a single specimen test, this higher result was discarded.

Total shrinkage was first measured for 106 days on a prism 70 × 70 × 280 mm demoulded at 1 day and exposed immediately to 50% RH and 20 °C. At 106 days, the prism reached 396 $\mu\varepsilon$. A simple model fitting total shrinkage yields

$$\varepsilon_{sh}(\hat{t}) = 450\frac{\hat{t}}{\hat{t}+13.8} \quad (1)$$

where $\hat{t} = t - 1$ day is drying time, $t$ is hydration time and the total asymptotic shrinkage reads 450 $\mu\varepsilon$. Assuming decomposition of total strain into autogeneous and drying parts, drying strain reaches 450–43 = 407 $\mu\varepsilon$ at 50% RH beyond approximately 2000 days.

This prism served also for calibrating moisture diffusivity but it turned out that the diffusivity is approximately 2.5 times higher when compared to the 100 × 100 × 400 mm prism and also to the deformation evolution of the ring test. For this reason, a larger prism 100 × 100 × 400 mm from RRT+ testing served for calibrating mass loss and total shrinkage (drying plus autogenous).

No basic creep measurements exist on RRT+ concrete, however, participants were asked to calibrate their models for VeRCoR's concrete, similar in the mix design and properties.

Total water content at the full saturation of mature VeRCoRs concrete was found as 165.3 kg·m$^{-3}$ whilst the desorption isotherm for mature concrete is depicted in Fig. 5.

### 2.1. Experiments for numerical benchmarking

Drying shrinkage presents the main driving force for the ring test. The benchmarking consists of validating free shrinkage of a prism and validating hoop strain on a steel ring in the ring test.

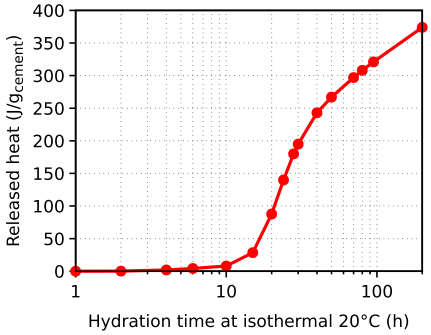


**Fig. 3.** Released heat from isothermal calorimetry.

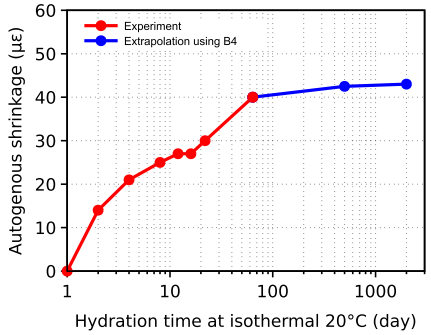


**Fig. 4.** Autogenous shrinkage.

The 100 × 100 × 400 mm prism hydrated under sealed conditions for 24 h. Afterwards, it was exposed to drying at four largest sides at 20°C and RH = 50%. The prism's mass loss and uni-axial free shrinkage served as benchmarking data. Only Team 1 did not participate in this benchmark as in this case the experimental results for shrinkage provided were used as an input for the ring model, i.e. for the calculation of the asymptotic shrinkage.

Fig. 6 illustrates ring test dimensions according to [7] with a photograph in Fig. 1. A notch 20 mm wide, made by inserting a steel plate, acted as a strain localizer for possible macrocrack formation. Concrete was cast to the ring at 20°C and sealed completely for 24 h to prevent any evaporation. After 24 h, horizontal plate and the outer ring were removed, outer side sealed with aluminum foil and concrete started drying from top and bottom surfaces. Ambient temperature was kept at 20 °C and external relative humidity stayed at 50% during the whole experiment taking 111 days. The inner ring was made from steel with E-modulus equal to 190 GPa and Poisson's ratio 0.30.

Four strain gages were attached to inner steel ring in mid-depth to monitor hoop strain, see Fig. 6. Sudden strain drop was unde-

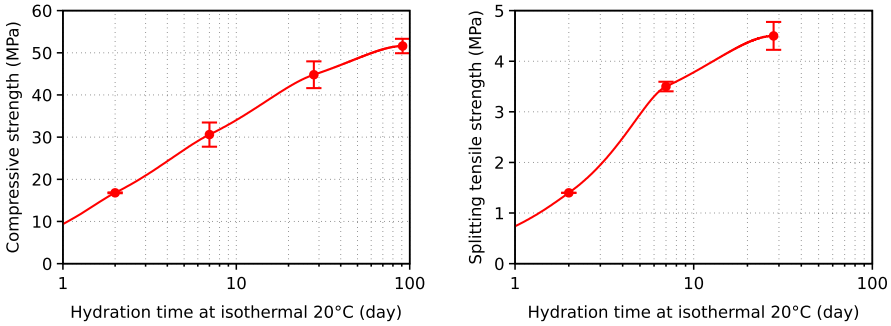


**Fig. 2.** Compressive and tensile strength of OC concrete.

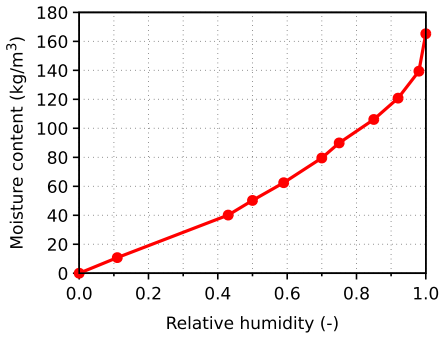


**Fig. 5.** Desorption isotherm for mature concrete.

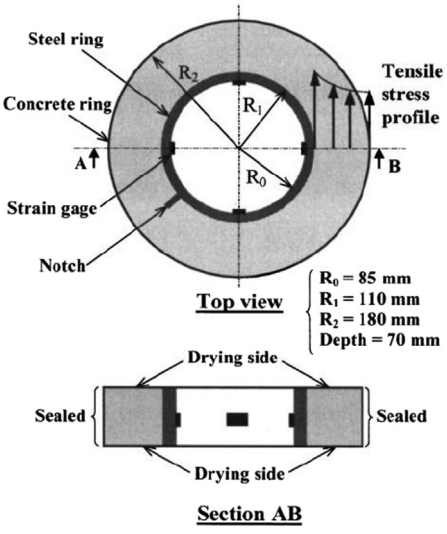


**Fig. 6.** Layout of the ring test, drying from top and bottom [7].

tected in this benchmark, which signalizes no macrocrack formation. The experimental campaign covered only one ring and one prism for this concrete.

## 3. Hygro-mechanical models

In this section, the governing and constitutive equations are briefly described to emphasize the various approaches of the six participating teams.

### 3.1. Moisture transport

For a single-fluid medium, the governing differential equation solves water mass balance in a unit volume [kg·m$^{-3}$s$^{-1}$] and reads [21]

$$\frac{\partial w}{\partial h}\frac{\partial h}{\partial t} = -\nabla \cdot J_w + w_n \frac{\mathrm{d}\alpha}{\mathrm{d}t} \tag{2}$$

where $h$ is the relative humidity [–], $\frac{\partial w}{\partial h}$ is the humidity-dependent moisture capacity [kg·m$^{-3}$], i.e. derivative of the moisture content $w(h)$ [kg·m$^{-3}$] given by the desorption isotherm. $J_w$ [kg·m$^{-2}$s$^{-1}$] represents the moisture flux, the sink term $w_n$ corresponds to non-evaporable water content for complete hydration [kg·m$^{-3}$] and $\alpha$ is the degree of hydration [-]. For the majority of cements, 1 kg of cement consumes approximately 0.23 kg of non-evaporable water at complete hydration [22]. The moisture flux is defined further by the constitutive law [21,23]

$$J_w = -c(h)\nabla h \tag{3}$$

where $c(h)$ [kg·m$^{-1}$s$^{-1}$] is the moisture permeability depending on the relative humidity.

Eq. (2) can be formulated in terms of $h$ as a state variable, assuming a linear desorption isotherm with a constant slope $k = \frac{\partial w}{\partial h}$ [21]. The resulting governing equation reads

$$\frac{\partial h}{\partial t} = -\nabla \cdot J_h + \frac{w_n}{k}\frac{\mathrm{d}\alpha}{\mathrm{d}t} \tag{4}$$

where $J_h$ [m·s$^{-1}$] represents the flux and the constitutive law reads

$$J_h = -D(h)\nabla h \tag{5}$$

where $D(h)$ [m$^2$s$^{-1}$] stands for diffusivity.

Team 1 used Eqs. (4) and (5) without hydration effects. In addition, Neumann's boundary condition controlled the surface flux [24]

$$J_s = h_w\left(h_{surf} - h_{air}\right) \tag{6}$$

where $h_{surf}$ represents relative humidity of concrete surface, $h_{air}$ is relative humidity of surrounding air, and $h_w$ is the hygric exchange coefficient as $6.37 \cdot 10^{-9}$ m·s$^{-1}$.

Team 2 uses model proposed by Künzel [23] in which the mechanism of moisture transport combines water vapor diffusion driven by pressure differences, liquid water conduction through micropores and capillary pores, and the surface diffusion in larger pores driven by the gradient in relative humidity. The experimental setup allows to directly compare this model with the model of Bažant and Najjar (see further Section 4.3) because the temperature was constant throughout the experiment and the desorption isotherm is almost linear on the investigated interval. Treating the moisture capacity as constant $\partial w/\partial h = k = 185.4$ kg·m$^{-3}$, the constitutive law for Eq. (4) can be rewritten to the form

$$J_h = -\underbrace{\left(D_w(h) + \frac{\delta\, p_{sat}}{\mu\, k}\right)}_{D(h)}\nabla h \tag{7}$$

in which the term in the parentheses is the humidity-dependent diffusivity, $D_w(h)$ [m$^2$s$^{-1}$] is the capillary transport coefficient, $\delta$ [kg·m$^{-1}$·s·Pa] is the water vapor permeability in air, $\mu = 400$ is the water vapor diffusion resistance factor, and $p_{sat}$ [Pa] is the saturation vapor pressure.

Team 3 uses a two-phase model of gas and water transport based on porous media theory. This team considered water consumption during hydration and its effect on decreasing evaporable water content as the hydration advances. The model used by Team 3 is derived from the fully-coupled hygro-thermo-chemo-mechanical model for early-age concrete by Gasch et al. [22]. For the benchmark a simplified version of this model was used by neglecting the influence of displacement on the moisture transport. Moisture flow is in the two-phase fluid medium governed by the mass balance of total water content and a dry air, which reads

$$\frac{\partial n S_w \rho_w}{\partial t} + \frac{\partial n(1-S_w)\rho_{wg}}{\partial t} = -\nabla \cdot \rho_w u_w - \nabla \cdot \rho_{wg} u_g - \nabla \cdot J_{wg} + w_n \frac{\mathrm{d}\alpha}{\mathrm{d}t} \tag{8}$$

$$\frac{\partial n(1-S_w)\rho_{dg}}{\partial t} = -\nabla \cdot \rho_{dg} u_g + \nabla \cdot J_{wg} \tag{9}$$

where $n$ is the age-dependent porosity, $S_w$ is the degree of liquid water saturation and $\rho_w$ is the density of water. The gas phase is a mixture of water vapour and dry air with the partial densities $\rho_{wg}$ and $\rho_{dg}$, respectively. The transport of moisture is determined by the Darcian flow of each phase, given by the velocities $u_w$ and $u_g$. A

diffusive flux $J_{wg}$ [kg·m$^{-2}$s$^{-1}$] in the gas phase is also considered. The capillary pressure $p_c$ is used as a state variable for Eq. (8) and the gas pressure $p_g$ for Eq. (9). Apart from fluid flow, the model also simultaneously solves for the temperature field and the degree of hydration $\alpha$. The latter is accounted for using a thermally activated affinity model and also gives a moisture sink, i.e. the last term in Eq. (8) and a heat source in the temperature field.

Team 4 uses Eqs. (2) and (3). Team 5 performs hygric calculations in two steps decoupling the effects of hydration and of drying on the water content evolution in time:

(a) During the first hours after casting and as long as the formwork is applied, it is assumed that concrete drying is prevented and that the water content evolution in time is mainly due to cement hydration [25]. So, the evaporable water content decreases linearly with the hydration rate $\alpha$. In the case of a typical CEM I cement type, this writes [26]

$$w(\alpha) = w_0 - 0.23 \cdot c \cdot \alpha \tag{10}$$

$w_0$ and $c$ are the initial water and cement contents in the design mix respectively [kg·m$^{-3}$].

(b) In the second step, and as the formwork is removed, it is assumed that concrete hydration has reached advanced state. Accordingly, the water content evolution in time is principally due to the hygric exchange between the hardened and partially saturated concrete and its surrounding ambient air. Hygric simulations consist of solving Eq. (2) with an initial water content state corresponding to the one after hydration ends (evaporable water in Eq. (10) when $\alpha$=1). Accordingly, in the second step, the term $w_n \frac{d\alpha}{dt}$ from Eq. (2) is neglected and hygric boundary conditions are prescribed according to Eq. (6) with $h_w = 3 \cdot 10^{-9}$ m·s$^{-1}$[27]. Team 6 considers water liquid permeation and vapour water diffusion mechanisms [28]. Effects of hydration on drying have been neglected.

### 3.1.1. Nonlinear permeability and diffusivity

All teams used non-linear moisture permeability or non-linear moisture diffusivity.

Team 1 uses moisture diffusion in Eq. (5) as described in [29]

$$D(h) = D_1 \left( \alpha_0 + \frac{1-\alpha_0}{1 + \left(\frac{1-h}{1-h_c}\right)^n} \right) \tag{11}$$

with $D_1 = 3.08 \cdot 10^{-10}$ m$^2$ s$^{-1}$, $\alpha_0 = 0.0967$, $h_c = 0.8$ and $n = 2$.

Team 2 uses the capillary transport coefficient from Eq. (7) estimated (for $w \leqslant w_f$) as

$$D_w(h) = 3.8 \left(\frac{A}{w_f}\right)^2 1000^{\frac{w(h)}{w_f}-1} \tag{12}$$

where $A = 5.103 \cdot 10^{-3}$ kg·m$^{-2}$s$^{-0.5}$ is the water absorption coefficient, and $w_f = 165.3$ kg·m$^{-3}$ is the moisture content at free saturation.

Team 3 uses age-dependent intrinsic permeability according to [30] and age-dependent relative permeability functions according to [31].

Teams 4 and 5 use a phenomenological exponential law for permeability in the following form [32]

$$C(w) = A \exp(Bw) \tag{13}$$

with $A = 1.1 \cdot 10^{-13}$m$^2$s$^{-1}$, $B = 0.06$ for Team 4 and $A = 3.12 \cdot 10^{-12}$m$^2$s$^{-1}$, $B = 0.05$ for Team 5.

Team 6 uses non-linear models for describing water liquid permeability [33] and vapour water diffusivity [34].

### 3.1.2. Desorption isotherm

Team 1 and Team 4 used a piecewise-defined isotherm from Fig. 5 for the whole drying period. Team 2 used linear desorption isotherm with slope k = 185.4 kg·m$^{-3}$ given by the ultimate value of the moisture loss. Team 3 used hydration degree dependent desorption isotherm, more accurate for early ages and showed in Fig. 7 [22,35].

Team 5 uses the model proposed in [28]

$$w(h) = w_0 \left(1 + (-a \log(h))^{\frac{1}{1-b}}\right)^b \tag{14}$$

which was fitted to the VeRCoRs mature curve with $a = 7.63, b = 0.33$, see Fig. 7. In that sense, the early age effect on the desorption curve is neglected as concrete is supposed to be exposed to drying once advanced hydration rate is achieved.

Team 6 uses the model proposed in [33]. Parameters have been fitted on the VeRCoRs mature curve from Fig. 5, without taking into account effects of hydration degree.

## 3.2. Mechanical behavior

All participants used small strain decomposition

$$\boldsymbol{\varepsilon} = \boldsymbol{\varepsilon}_e + \boldsymbol{\varepsilon}_v + \boldsymbol{\varepsilon}_{as} + \boldsymbol{\varepsilon}_{ds} + \boldsymbol{\varepsilon}_f \tag{15}$$

where the strains represent part of elastic, viscous, autogenous shrinkage, drying shrinkage and fracturing strain if applicable. Autogenous shrinkage is experimentally known from Fig. 4.

Creep models describe long-term stress/strain evolution and they make use of a relaxation equation in an incremental form [36]

$$\Delta\overline{\boldsymbol{\sigma}} = \overline{\mathbf{E}}\left(\Delta\boldsymbol{\varepsilon} - \Delta\boldsymbol{\varepsilon}'' - \Delta\boldsymbol{\varepsilon}_{as} - \Delta\boldsymbol{\varepsilon}_{ds} - \Delta\boldsymbol{\varepsilon}_f\right) \tag{16}$$

where $\overline{\mathbf{E}}$ is the incremental stiffness tensor and $\Delta\boldsymbol{\varepsilon}''$ contains strain history. Aging compliance functions for basic and drying creep are hidden in $\overline{\mathbf{E}}$ and $\boldsymbol{\varepsilon}''$. The effective stress, $\overline{\boldsymbol{\sigma}}$, represents stress carried by a certain effective intact fraction of material in the sense of damage mechanics.

Team 1 used the method described in [37] where computed moisture, $h$, is transformed into a field of unrestrained shrinkage $\varepsilon_{sh}$

$$\varepsilon_{ds}(h) = \varepsilon_{ds,\infty}\left[0.97 - 1.898(h - 0.2)^3\right] \tag{17}$$

with an asymptotic shrinkage value $\varepsilon_{ds,\infty} = 457\mu\varepsilon$.

Teams 2 and 6 assumed linear relationship between drying shrinkage strain rate and relative humidity $h$ rate using a shrinkage factor $k = 850\mu\varepsilon$ and $k = 800\mu\varepsilon$, respectively

$$\dot{\varepsilon}_{ds} = k\dot{h} \tag{18}$$

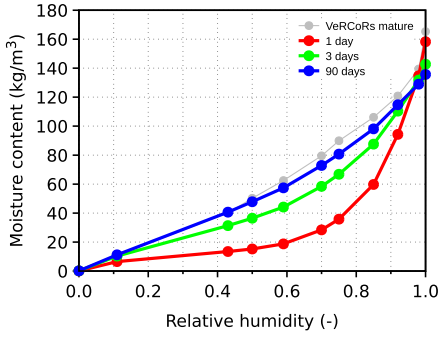


**Fig. 7.** Age-dependent desorption isotherm used by Team 3 and comparison with VeRCoRs isotherm from Fig. 5.

Team 3 used the effective stress principle to calculate the drying shrinkage [38] (not to be confused with the effective stress in damage mechanics). Using this approach drying of the material causes an internal load on the solid skeleton that results in a contraction of the material. Apart from an instantaneous deformation, this internal load contributes to the creep deformation. Hence, the shrinkage strain is considered as the total deformation, i.e. instantaneous and creep, when the specimen is exposed to no external loads. This deformation thus also include the autogenous shrinkage, which is described by a decreasing humidity due to the chemical binding of pore water during hydration.

Teams 4 and 5 assumed a linear relationship between the drying shrinkage strain and the water content $w$ [kg·m$^{-3}$] as prescribed in [39][40]

$$\dot{\varepsilon}_{ds} = k\dot{w} \tag{19}$$

with a shrinkage factor $k = 4.45\mu\varepsilon/(\text{kg}\cdot\text{m}^{-3})$ for Team 4 and $k = 5.4\mu\varepsilon/(\text{kg}\cdot\text{m}^{-3})$ for Team 5.

### 3.2.1. Creep and E modulus

All teams calibrated their models for aging basic creep at $t' = 1$ and 3 days with the results presented in Fig. 8. Those compressive creep tests were carried out in the framework of VeRCoRs project; cylindrical specimens 160 mm in diameter and 1 m long were loaded by uniaxial stress of 12 MPa [41]. No experimental data were used for validating drying creep, non-linear creep or creep in tension.

Validation of static elastic modulus stems from a short-term creep compliance function

$$E(t) = \frac{1}{J(t + 0.01\text{day}, t)} \tag{20}$$

whilst Fig. 9 shows validation for six Teams with relative deviation up to 35%.

Team 1 used the Double Power Law (DPL)[42] to account for basic creep while neglecting drying creep. The model was calibrated against experimental data from Fig. 8. Corresponding parameters were $\phi_1 = 0.39, m = 0.2$ and $n = 0.15$. The evolution of elastic modulus with time was accounted for using the formulation inherent in MC2010 [43].

Team 2 used a calibrated B4 model [20] with MPS extension [44] and with zero size-effect on drying creep [45]. The following parameters were used: $q_1 = 23 \cdot 10^{-6}\text{MPa}^{-1}, q_2 = 40 \cdot 10^{-6}\text{MPa}^{-1}$, $q_3 = 2.4 \cdot 10^{-6}\text{MPa}^{-1}, q_4 = 6 \cdot 10^{-6}\text{MPa}^{-1}, \tilde{p} = 1, k_3 = 1$, $\varepsilon_{au\infty} = -50 \cdot 10^{-6}$, $\tau_{au} = 1.04$ days. The effect of drying on equivalent hydration time and thus on aging was neglected by setting $\alpha_E = 0.0$.

Team 3 used a creep model based on the MPS theory as presented in [22]. The following parameters are used: $q_1 = 23 \cdot 10^{-6}\text{MPa}^{-1}$, $q_2 = 12.2 \cdot 10^{-6}\text{MPa}^{-1}, q_4 = 7.6 \cdot 10^{-6}\text{MPa}^{-1}, m = 2, p = 2, \mu_C = 2.16 \cdot 10^{-9}$ MPa$^{-1}$day$^{-1}$. Parameter $m$ defines the solidification as a function of the degree of hydration $\alpha$ and $\mu_C$ controls the influence of drying creep. The effect of drying on the creep is determined by the evolution of the degree of hydration and by reducing the rate of microstructral bonds with a factor $S_w^2$.

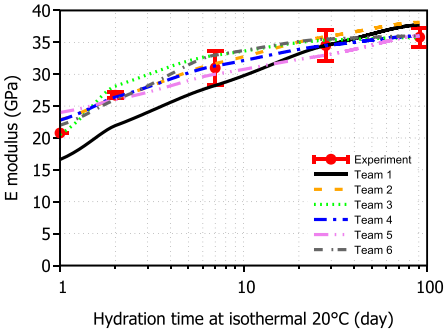


**Fig. 9.** Validation of ageing E modulus.

Team 4 used two aging Kelvin units based on Granger's model [46] in the form [$\mu\varepsilon$/MPa]

$$J(t,t') = k(t')\left[23\left(1 - \exp\left(\frac{t-t'}{2\text{ d}}\right)\right) + 50\left(1 - \exp\left(\frac{t-t'}{150\text{ d}}\right)\right)\right] \tag{21}$$

$k(t')$ is an aging function defined as $k(t') = \left(28^{0.2} + 0.1\right)/(t'^{0.2} + 0.1)$ if $t' \leq 28$ days, and $k(t') = 1$ if $t' > 28$ days [47].

Team 5 uses a generalized version of the Burgers model in [48] to include the effect of early age on the viscoelasticity of concrete as defined in [49]. Creep Poisson effects [50] (different than the elastic one), long term creep, thermo-activation and drying effects (drying creep is supposed proportional to the drying kinetic and the stress level) are also accounted for. The full version of the model is detailed in [26].

Team 6 model is an extension of the Burgers models [51]. Basic creep is driven by effective stresses. Apparent stiffness and viscosity parameters are made dependent on hydration degree (description of early-age creep), equivalent time (description of long term creep), temperature (thermal activation following an Arrhenius law) and saturation degree (creep strains are proportional to this variable, i.e. there is no basic creep of a fully-dried concrete). Drying creep is modelled by assuming that it is proportional to drying shrinkage and the effective stresses [39]. The extension to 3D is achieved by using a constant creep Poisson ratio, equaling to the elastic one 0.2 for both basic and drying creep.

### 3.2.2. Fracture models

Instantaneous material fracture models, sometimes called short-term ones, describe quasi-static concrete softening beyond elastic limit.

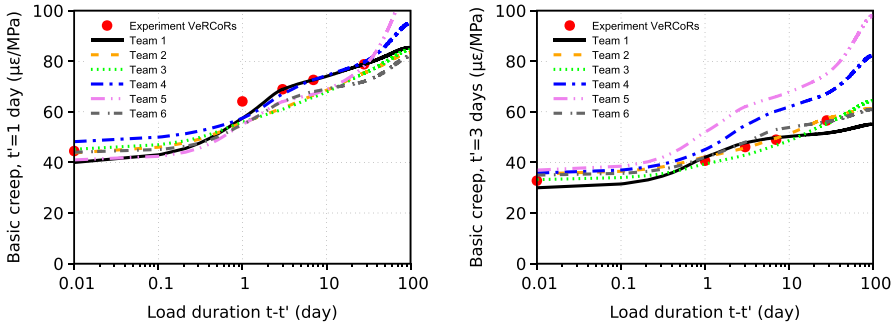


**Fig. 8.** Basic creep at 1 and 3 days.

Team 1 and Team 2 implemented a smeared crack approach to simulate fracture with strain decomposition of the total strain tensor to elastic and crack components $\varepsilon = \varepsilon_e + \varepsilon_{crack}$ [52]. Crack formation and propagation in concrete was modelled using stress-strain tension model with linear (Team 1) and exponential (Team 2) softening based on the Crack Band Theory [53]. The enclosed area in the stress-strain diagram is equal to the ratio of the fracture energy $G_f$ (estimated herein in accordance to MC2010 [43]), and the characteristic length of the current finite element, $h$, adopted from the mesh discretisation. In this case, $h$ depends on finite element's size in order to reduce dependency of the simulation on mesh refinement. This is generally a widely employed approach also explained elsewhere [54,55]. Both teams used the average values for splitting tensile strength test in Fig. 2.

Team 3, Team 5 and Team 6 use isotropic-based damage model with the relation to nominal stress as

$$\boldsymbol{\sigma} = (1 - D)\overline{\boldsymbol{\sigma}} \tag{22}$$

where the damage $D$ is linked to the equivalent tensile strain. Team 3 and Team 6 took the average values for splitting tensile strength test in Fig. 2.

Team 5 uses a stochastic-based isotropic, unilateral and energy-regularized damage model [26]. In this model, the tensile damage strain threshold is defined as the ratio of the tensile strength to the Young's modulus:

(a) An energetic size effect law which relates concrete's tensile strength to its effective volume under tensile loads as shown in Eq. (23) [56]. Accordingly, the ring's tensile strength is expected to be 3% higher than the one of the split test specimen. Therefore, one can assume that the specimen used for the split test is representative of the ring's specimen in the sense of energetic size effects considered in [56].

$$R_t(V_{ring}) = R_{t,ref}(V_{ref}) \cdot \left(\frac{V_{ring}}{V_{ref}}\right)^{-\frac{1}{m}} \tag{23}$$

$R_t(V_{ring})$ and $R_t(V_{ref})$ the tensile strength values of the ring concrete element of an effective volume $V_{ring}$ estimated around 200 cm$^3$ [26] and of the reference split test specimen of an effective volume $V_{ref}$ estimated around 300 cm$^3$ [56]. $m$ the Weibull modulus estimated at 12 for a tensile strength coefficient of variation around 10%. In explicit terms, the mean value of the strain tensile damage threshold of the ring is evaluated at 128 $\mu\varepsilon$ for a mature concrete. Naturally, this threshold evolves with the hydration rate in line with the evolution of the Young's modulus and tensile strength in Figs. 2 and 9.

(b) A statistical size effect which describes the spatial scattering of the strain tensile damage threshold due to concrete's intrinsic heterogeneity. In this work, and similarly to the reference analysis in [26], this is modeled by associating a random field to the Young's modulus property (lognormal field spatially correlated using a Gaussian function with a metric fluctuation length and a coefficient of variation estimated at 10%). Eventually, the same coefficient of variation (i.e. 10%) is observed for the strain tensile damage threshold around a mean value of 128 $\mu\varepsilon$ for a hardened state.

The used model also accounts for the contribution of creep to the concrete damage [57]. In this contribution, it is assumed that 40% [26] of the creep equivalent tensile strain contributes to concrete damage in addition to the elastic equivalent tensile strain [58].

Team 6 based the fracture model on Mazars [59]. Several features have been added with constitutive equations summarized elsewhere [60]. The model has been adapted to early-age evolution, regularized by using an energetic approach introducing the finite element size (like Team 1 and 2) and extended to account for creep/cracking coupling (like Team 5). In order to take into account part of the heterogeneity of concrete and to have a random crack initiation, a spatially correlated random field of tensile strength (coefficient of variation of 10% and a correlation length of 3 cm) has been used by adopting the turning band method [61].

Table 2 summarizes state variables and material models for all teams. Constitutive models and their parameters remained the same for both prism and ring. Indicative computational times are listed as well.

## 4. Benchmark results and discussion

### 4.1. Validation of drying prism

The first part considered the simulation of a 100 × 100 × 400 mm prism which was exposed to 50% RH after

**Table 2**
Modeling details of each team.

| Item | Team 1 | Team 2 | Team 3 | Team 4 | Team 5 | Team 6 |
|---|---|---|---|---|---|---|
| State variable(s) | $h$ | $h$ | $p_c + p_g$ | $w$ | $w$ | $S_l$ |
| Moisture diffusivity type | Power [29] | Power - Künzel [23] | | | | Vapour water diffusion + |
| Moisture permeability type | | | Power | Exponential | Exponential [32] | Liquid water permeation |
| Desorption isotherm | N/A | Linear VeRCoRs | Age-dependent | VeRCoRs | Log-power [28] | Power [33] |
| Creep model | Double-power law | Calibrated B3/B4 with MPS theory | Calibrated B3 with MPS theory | Two ageing Kelvin units | Burgers model (Kelvin and Maxwell units in series) [48] | Ageing Burgers model [51] |
| Material model for fracture | Multidirectional fixed crack model | Multidirectional fixed crack model | Isotropic damage model | - | Stochastic isotropic unilateral damage model [26] | Isotropic damage model[51] |
| Software | Diana, iDiana, MATLAB | OOFEM | COMSOL | Code Aster | Code Aster | Cast3m |
| Degrees of freedom for prism | N/A | 18207 | 23338 | 14869 | 17001 | 10000 |
| Computation time for prism | N/A | 18 min | 3.5 min | 2 min | 3.5 min | 3 min |
| Number of time steps for prism | N/A | 55 | 91 | 80 | 50 | 60 |
| Degrees of freedom for ring | 46704 | 55944 | 74896 | 300 | 51396 | 84000 |
| Computation time for ring | 20 min | 42 min | 10 min | 5 min | 21 min | 60 min |
| Number of time steps for ring | 322 | 58 | 83 | 100 | 250 | 120 |

1 day of sealed hydration. The mass loss served for calibrating kinetics and was normalized per 1 $m^3$, see Fig. 10. Mechanical response was assessed as well; Fig. 11 reflects total longitudinal shrinkage on the prism axis, including autogenous shrinkage, drying shrinkage, creep and induced fracture.

Teams 2–6 predicted reasonably well mass loss of the prism, as shown in Fig. 10, as well as its total shrinkage, depicted in Fig. 11. Only Team 1 did not provide simulations of the unrestrained prism, as explained previously in Section 2.1.

In order to illustrate the prism behavior, Fig. 12 shows 1/8 model at 1 week, 1 month and 1 year of drying. There are obvious deformations due to drying, cross-section deplanation, surface cracking and finally, closed cracks in 1 year.

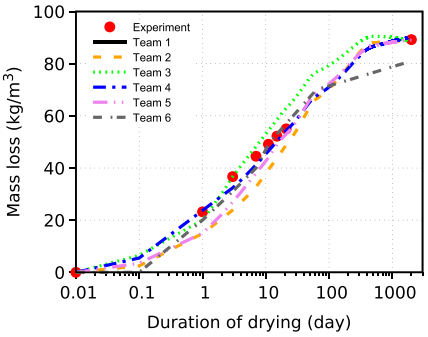


**Fig. 10.** Mass loss of the drying prism.

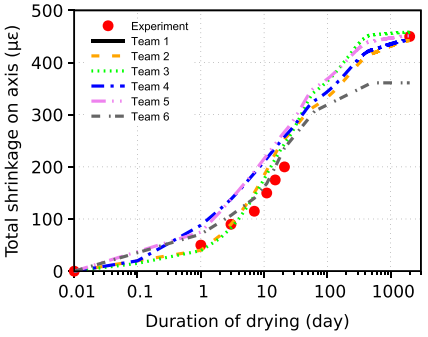


**Fig. 11.** Total shrinkage on the prism axis.

### 4.2. Validation of the ring

The same transport and mechanical models served further for the validation of the ring tests. All participants used a 3D model except Team 4 which used axisymmetric model without any damage. Fig. 13 shows used meshes in hygro-mechanical models. In addition, Teams 2, 3, 5, 6 considered the notch in the models corresponding to the experiment. Perfect bond existed between steel ring and concrete, without any interface elements. The validation considered hoop steel strain, as showed in Fig. 14.

Up to 7 days, all teams predicted similar tangential strains. Between 7–40 days, strains are more scattered due to progressing drying and damage. Strain acceleration after 7 days is generally higher than model predictions. One reason is probably surface cracking; the models lack strong hygro-mechanical coupling where cracks accelerate moisture transport. Another reason stems from using isotropic material damage model by Team 3 and Team 6 which adds artificial radial compliance due to the softening in hoop direction. Team 4 introduced no strength limits hence the steel strain leads to overprediction, see Fig. 14.

Between 40 and 111 days, small tangential strain decrease occurs in the ring test but without any macrocrack. There is apparently a nonlinear (tertiary) creep where tensile stress is close to material strength. The results of Teams 1–3 and Team 5 followed such behavior, however, validated strain attenuated rather slowly. Team 4 showed higher strains due to missing strength limits and Team 6 gave no strain drop even though material law accounts for creep-induced damage directly, see Fig. 16. Only Team 5

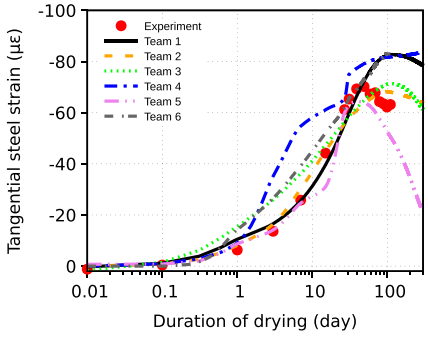


**Fig. 14.** Hoop strain validation of the ring test.

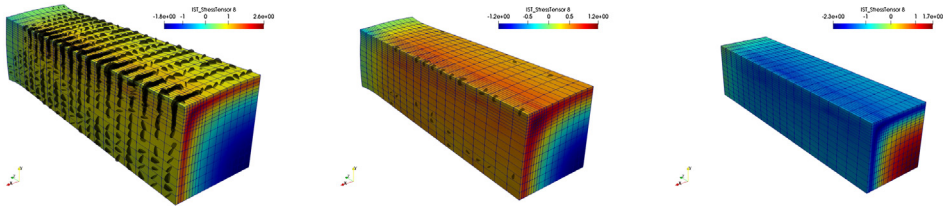

**Fig. 12.** Deformed shape of a prism after 1 week, 1 month and 1 year of drying. Color bar displays longitudinal stress, black disks indicate cracks which are below 5 μm and close finally.

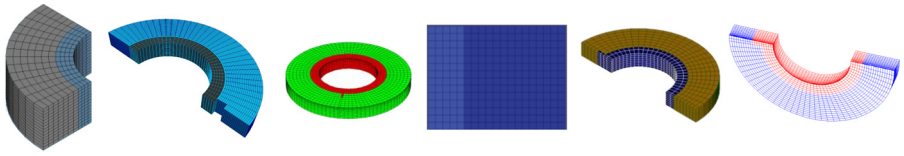

**Fig. 13.** Meshes used by Teams 1–6.

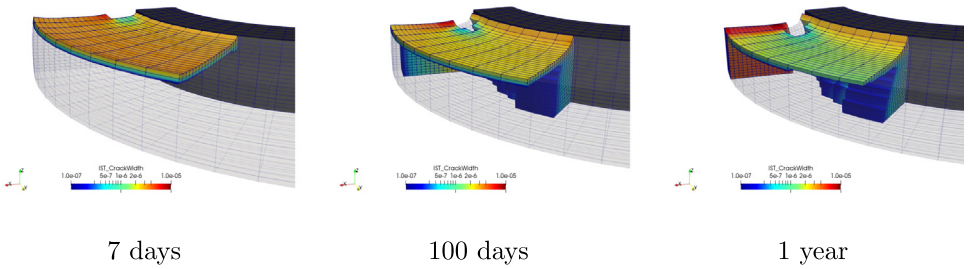


**Fig. 15.** Evolution of the crack width in the concrete ring of drying according to Team 2. Only elements with cracks width exceeding 0.1 μm are shown in 1/16 of the concrete ring; the notch is on the rear left side in each picture.

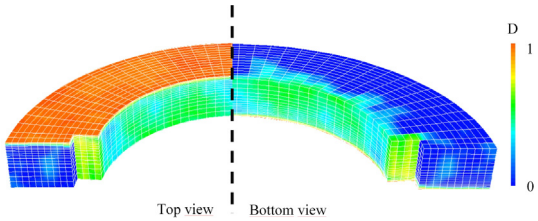


**Fig. 16.** Damage at 100 days according to Team 6.

demonstrated significant strain localization around ring's notch, see Fig. 17. Every model predicted correctly ring behavior without its rupture in a single macrocrack.

More details for Teams 2, 5, 6 follows. Damage occurred immediately after beginning of drying on horizontal surfaces, growing later to the depths of a few mm, see Figs. 15 and 16. Owing to perfect concrete-steel bond, concrete damage is relatively easily introduced in the adjacent zone close to the steel ring. The notch in the ring created small strain localization but, due to high strain gradient, it did not propagate to a macrocrack even after experimental 111 days. In this regard, the notch seems unnecessary in the ring test and also in the models.

One should note that the exposed result in Fig. 16 is one realization coming from random fields and cannot be seen as a mean response. Indeed, random sampling methods are required to compute several ring simulations using several random fields before achieving statistical analysis and deriving the mean response and its variation. The numerical cost of such work remains high as mentioned in [26] which is the main drawback of the used stochastic-based damage model in opposition to the main advantage of simulating realistic random cracking patterns.

In terms of stress evolution, the Teams provided blind predictions summarized in Fig. 18. Two material points served for mutual comparison: a) proximal point close to the steel ring (inner circumference of concrete ring) and distal point close to the vertical exterior (outer circumference of the concrete ring), both located in the mid-height. Hoop stresses are known to decrease from the ring outwards using analytical elastic solution for the condition of top and bottom drying [7]. This is obtained numerically as well for all Teams in Fig. 14.

Up to 30 days, proximal and distal hoop stresses work similarly for all Teams which took into account concrete tensile strength (Team 4 set no strength limits). The similarity stems from only superficial damage located on exposed drying surfaces. After 30 days, the results are scattered similarly as for hoop steel strain with the same arguments. Moreover, Team 5 and Team 6 do not reach the tensile strength of the concrete due to a damage criteria in strain and the coupling with creep. Team 5 nicely demonstrates that the decrease of stresses is directly linked to the unloading due to strain localization and crack propagation.

It is worth noting that for models with damage, the concrete stress prediction is highly affected by the cracks and therefore is not homogeneous even in the orthoradial direction.

### 4.3. Influence of steel-concrete contact

All Teams considered perfect contact between the restraining steel ring and the outer concrete. Team 2 further investigated imperfect contact and its impact on displacements, stresses and strains. Four contact scenarios were studied:

**PERFECT** – a perfect connection between steel and concrete used by all Teams.
**INT** – interface elements allowing only opening.

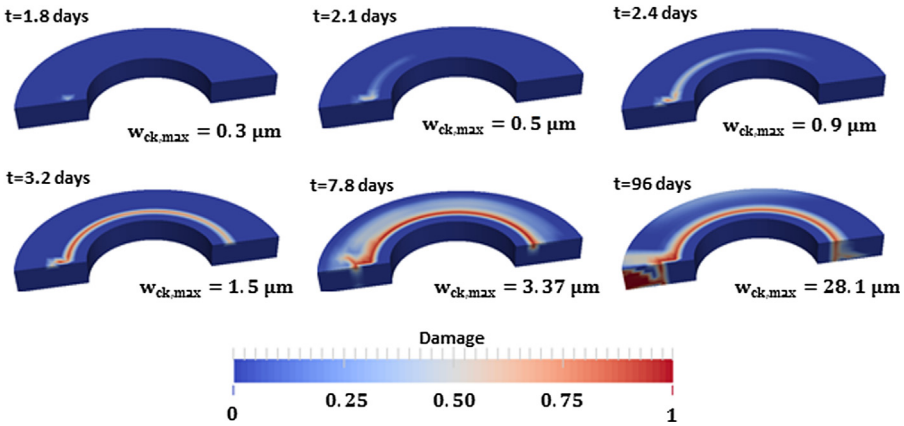


**Fig. 17.** Damage evolution according to Team 5.

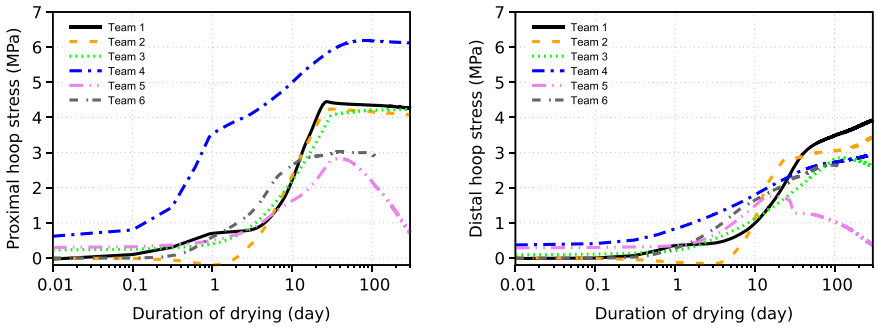


**Fig. 18.** Proximal and distal hoop stress in concrete in mid-height, blind predictions.

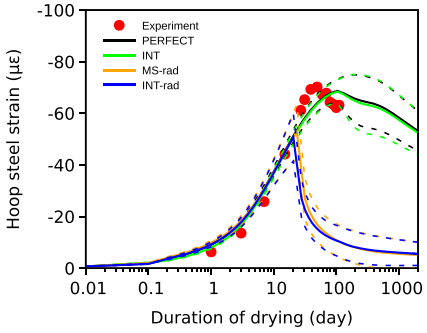


**Fig. 19.** Evolution of strain on the inner surface of the steel ring for different contacts, displayed with solid lines. Dashed lines show bounds in other mid-height points.

**MS-rad** – master–slave connection in the radial direction allowing free hoop slip but not opening.
**INT-rad** – interface elements allowing opening and free hoop slip.

Fig. 19 shows the results for the four scenarios. It turned out that *MS-rad* and *INT-rad* act similarly since concrete can freely slip from steel, cracks at the notch localize and the steel ring rapidly unloads. Solid lines in Fig. 19 correspond to the average of two strain measurements evaluated 45° and 135° away from the notch, according to Fig. 6. This difference is induced by the notch and increases with decreasing friction between steel and concrete. It also points to the fact that friction plays a role in experiment, even with lubricated steel ring. Dashed lines show bounds in other mid-height points.

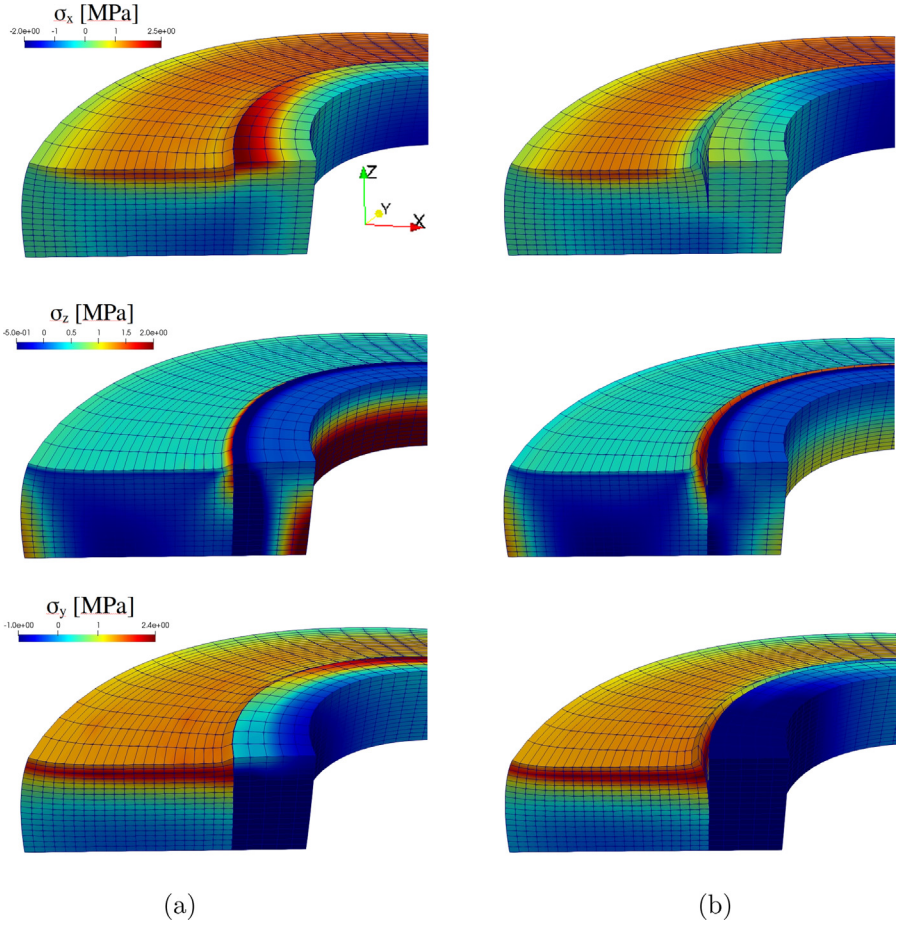


**Fig. 20.** Distribution of normal stresses in the concrete and steel ring after 1.5 days of drying in the model. (a) PERFECT and (b) INT interface elements between the concrete and steel rings according to Team 2. Top row: $\sigma_x$ (radial direction on the front face), middle row: $\sigma_z$ (vertical direction), bottom row: $\sigma_y$ (hoop direction on the front face).

*PERFECT* and *INT* lead to similar results in Fig. 19 for hoop strains/stresses. However, vertical stress differs substantially, see Fig. 20. *PERFECT* leads to unrealistic bending of the steel ring and to the development of spurious stresses. *INT* seems to provide the most realistic response, especially if triaxial stress/state is of interest.

### 4.4. Suitable experimental data for calibration

Team 2 examined the sensitivity of the structural response to the parameters controlling creep and to the choice of the model for moisture transport.

In the simulation of the free shrinkage the self-equilibrated stresses originating from drying shrinkage are highly nonuniform over the cross-section, yet the resulting evolution of the longitudinal shrinkage (Fig. 21a) is in the case of the examined MPS model almost insensitive to the choice of the material parameters $k_3$ and $\alpha_E$ which are responsible of drying creep and humidity-affected aging, respectively. The significance of these parameters arises with increasing stiffness of the external restraint, such as in the case of the ring test, see Fig. 21b.

It must be noted that the optimum fit has been obtained with $\alpha_E = 0$ and $k_3 = 1$ but their default/usual values are 10 and around 20, respectively. For this reason, a realistic distribution of stresses originating from drying can be achieved only if the material parameters are identified from separate experiments on both free and restrained shrinkage.

Fig. Fig. 22a presents two distinctly different diffusivity functions, the blue curve is calibrated from the Künzel's model, the green curve corresponds to the model proposed by Bažant and Najjar (B-N) with parameters $D_1 = 4.63 \cdot 10^{-10}\mathrm{m^2 s^{-1}}, \alpha_0 = 0.1$, $h_c = 0.75, n = 8$. Surprisingly, even when the distribution of relative humidity is different, the resulting structural response in both cases is very similar, see Fig. 21. The deficiencies of the B-N model emerge when the back-calculated moisture loss is compared to the experimental data, see Fig. 22b; the moisture loss is initially very underestimated. However, if the moisture loss data is not available, or it is not used for the calibration of the shrinkage kinetics, the above-mentioned discrepancy can be over-weighed by the robustness, simple calibration, and fast convergence of the B-N model.

## 5. Conclusion

This benchmark used available experimental data generated in the RRT + programme of COST Action TU1404. Compliance to calibration of selected experimental data was a prerequisite for successful macroscopic validation of the ring test. The results from five participants showed:

1. Drying shrinkage presented dominant loading in studied concrete; asymptotic drying shrinkage reached 407 $\mu\varepsilon$ while autogeneous shrinkage only 43 $\mu\varepsilon$. Mass loss on accompanying prism served for calibration of drying kinetics, optimally with the same cross-section as the ring. Beyond a known desorption isotherm, separate permeability tests at various humidity would improve calibration of nonlinear moisture transport models. Alternatively, measured unrestrained shrinkage can be used as the driving force in the hygro-mechanical simulation and satisfactory results are obtained.

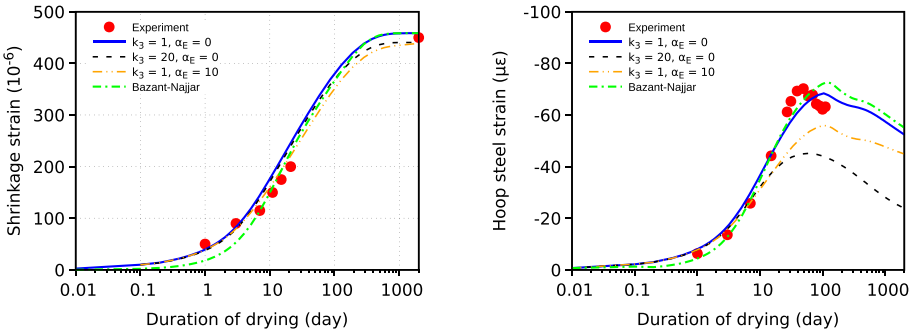


**Fig. 21.** Influence of the material model on the evolution of (a) longitudinal strain in drying prism, (b) hoop strain on the inner face of the steel ring.

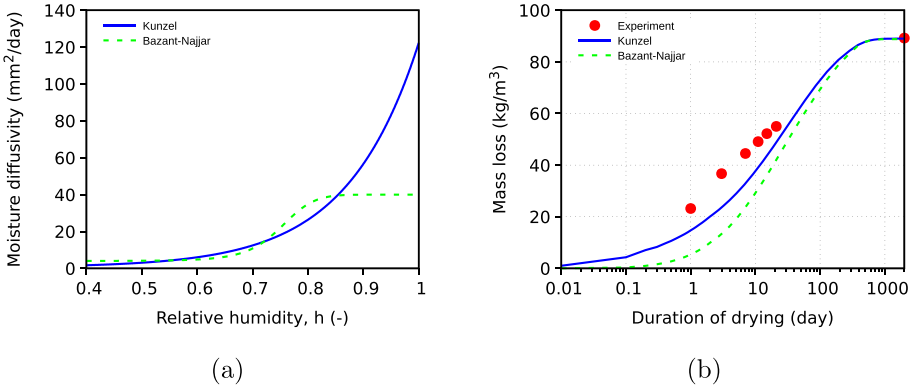


**Fig. 22.** Calibrated functions of (a) moisture diffusivity and (b) calculated evolution of moisture loss described by the models of Bažant-Najjar and Künzel (linear moisture capacity assumed) (Team 2).

2. Aging creep represents sensitive constitutive law for stress evolution with impact on concrete fracture. Any calibrated aging material model is found sufficient.
3. Notch in the concrete ring has negligible effect both experimentally and numerically as a strain localizer. Concrete-steel interface prevents hoop slip which prevents strong strain localization to the notch. Therefore, even simple 2D axisymmetric models provide good accuracy.
4. Stochastic fracture modeling led to similar global behaviour as homogeneous simulations during the first days. Damage initiation and propagation appeared generally earlier due to the existence of weaker material points. In this regard, measurement of spatial variability of tensile strength and Young's modulus would enhance model predictions.
5. Behavior of the ring test is influenced by the type of interface between steel ring and concrete. Frictionless connection triggers earlier strain localization than was observed in the experiment. When the global behavior is assessed in terms of the hoop strain, it does not matter whether the interface opens or not.
6. Hygro-mechanical models performed generally well on the global scale even with different model assumptions. However, local hoop stresses greatly varied among models and depended on selected locations. This suggests the need for detailed monitoring of local stress/strain data.

## Declaration of Competing Interest

None.

## Acknowledgements

The authors would like to acknowledge networking support by the COST Action TU1404 (www.tu1404.eu) and experimental work carried by involved partners. Czech Technical University acknowledges support by Technology Agency of the Czech Republic under project TH03020404 and by Czech Science Foundation under project 19-20666S. The team of UMinho acknowledges the support of FCT/FEDER(COMPETE2020) through the research project IntegraCrete PTDC/ECM-EST/1056/2014 (POCI-01-0145-FEDER-016841). The team from KTH acknowledges the support of the Swedish Hydropower Centre (SVC). The team from 3SR laboratory acknowledges the funding from the industrial chair PERENITI and the valuable contribution of professors Frédéric Dufour and Julien Baroth to the results' analysis. The contents of this paper reflect the views of the authors, who are responsible for the validity and accuracy of presented data, and do not necessarily reflect the views of their affiliated organizations.

## References

[1] A. Vaysburd, P. Emmons, B. Bissonnette, M. Pigeon, Some aspects of evaluating cracking sensitivity of repair materials, in: K. Kovler, A. Bentur (Eds.), International RILEM Conference on Early Age Cracking in Cementitious Systems, RILEM Publications SARL, 2003, pp. 169–185.
[2] M. Briffaut, F. Benboudjema, J.-M. Torrenti, G. Nahas, Numerical analysis of the thermal active restrained shrinkage ring test to study the early age behavior of massive concrete structures, Eng. Struct. 33 (4) (2011) 1390–1401, https://doi.org/10.1016/j.engstruct.2010.12.044.
[3] R. Burrows, The visible and invisible cracking of concrete, Americal Concrete Institute (1998).
[4] P. Krauss, E. Rogalla, Transverse cracking in newly constructed bridge decks, Report 380, Transportation research board, 2101 Constitution avenue, Washington, D.C., 1996..
[5] W.J. Weiss, S.P. Shah, Restrained shrinkage cracking: The role of shrinkage reducing admixtures and specimen geometry, Mater. Struct. 34 (246) (2002) 85–91.
[6] X. Wang, K. Wang, F. Bektas, P. Taylor, Drying shrinkage of ternary blend concrete in transportation structures, J. Sustainable Cement-Based Mater. 1 (1–2) (2012) 55–66.
[7] P. Turcry, A. Loukili, K. Haidar, G. Pijaudier-Cabot, A. Belarbi, Cracking tendency of self-compacting concrete subjected to restrained shrinkage: Experimental study and modeling, J. Mater. Civ. Eng. 18 (1) (2006) 46–54, https://doi.org/10.1061/(ASCE)0899-1561(2006)18:1(46).
[8] F. Kanavaris, M. Azenha, M. Soutsos, K. Kovler, Assessment of behaviour and cracking susceptibility of cementitious systems under restrained conditions through ring tests: a critical review, Cement Concr. Compos. 95 (2019) 137–153, https://doi.org/10.1016/j.cemconcomp.2018.10.016.
[9] M. Azenha, Numerical Simulation of the Structural Behaviour of Concrete since its Early Ages Ph.D. thesis, University of Porto, Porto, Portugal, 2009.
[10] F. Kanavaris, Early Age Behaviour and Cracking Risk of Concretes Containing ggbs Ph.D. thesis, Queen's University Belfast, Belfast, UK, 2017.
[11] A. Bentur, K. Kovler, Evaluation of early age cracking characteristics in cementitious systems, Mater. Struct. 36 (2003) 183–190.
[12] A.B. Hossain, J. Weiss, The role of specimen geometry and boundary conditions on stress development and cracking in the restrained ring test, Cem. Concr. Res. 36 (1) (2006) 189–199, https://doi.org/10.1016/j.cemconres.2004.06.043. URL: http://www.sciencedirect.com/science/article/pii/S0008884605000463.
[13] Z.C. Grasley, M.D. D'Ambrosia, Viscoelastic properties and drying stress extracted from concrete ring tests, Cement Concr. Compos. 33 (2) (2011) 171–178, https://doi.org/10.1016/j.cemconcomp.2010.10.014. URL: http://www.sciencedirect.com/science/article/pii/S0958946510001733.
[14] J. Moon, F. Rajabipour, B. Pease, J. Weiss, Quantifying the influence of specimen geometry on the results of the restrained ring test, Journal of ASTM International 3 (8) (2006) 171–178, https://doi.org/10.1520/JAI100436. 1–14.
[15] W. Dong, X. Zhou, Z. Wu, A fracture mechanics-based method for prediction of cracking of circular and elliptical concrete rings under restrained shrinkage, Eng. Fract. Mech. 131 (2014) 687–701, https://doi.org/10.1016/j.engfracmech.2014.10.015. URL: http://www.sciencedirect.com/science/article/pii/S0013794414003373.
[16] R. Nakhoul, O. Pierard, Modeling restrained shrinkage induced cracking in concrete rings using the thick level set approach, Appl. Sci. 8 (4) (2018), https://doi.org/10.3390/app8040488.
[17] E. Oukhemanou, S. Desforges, E. Buchoud, S. Michel-Ponnelle, A. Courtois, Vercors mock-up: Comprehensive monitoring system for reduced scale containment model, in: G. Herve (Ed.), International Conference on Technological Innovations in Nuclear Civil Engineering (TINCE), Paris, France, 2016, pp. 1–10.
[18] H. Samouh, E. Roziére, A.Z. Bendimerad, A. Loukili, Viscoelastic properties of self-consolidating concrete: Influence of the sustainable approach, Cement Concr. Compos. 86 (2018) 273–287, https://doi.org/10.1016/j.cemconcomp.2017.11.020. URL: http://www.sciencedirect.com/science/article/pii/S0958946516307600.
[19] G. Trtnik, M. Serdar, S. Nanukuttan, et al., RRT+ Main phase of the Extended Round Robin Testing programme for TU1404. Testing protocols., report, TU1404 (11 2016)..
[20] RILEM Technical Committee TC-242-MDC (Z.P. Bažant, chair), Model B4 for creep, drying shrinkage and autogenous shrinkage of normal and high-strength concretes with multi-decade applicability (RILEM Technical Committee TC-242-MDC multi-decade creep and shrinkage of concrete: material model and structural analysis)., Materials and Structures 48 (2015) 753–770..
[21] Z.P. Bažant, L.J. Najjar, Nonlinear water diffusion in nonsaturated concrete, Mater. Struct. 5 (25) (1972) 3–20.
[22] T. Gasch, D. Eriksson, A. Ansell, On the behaviour of concrete at early-ages: a multiphase description of hygro-thermo-chemo-mechanical properties, Cem. Concr. Res. 116 (2019) 202–216, https://doi.org/10.1016/j.cemconres.2018.09.009.
[23] H. Künzel, Simultaneous Heat and Moisture Transport in Building Components, IRB, Stuttgart, 1995.
[24] M.A.M. Oliveira, P. Lourenco, Simulation of humidity fields in concrete: experimental validation and parameter estimation, J. Adv. Concrete Technol. 73 (2015) 214–229.
[25] T.C. Powers, T.L. Brownyard, Studies of the physical properties of hardened Portland cement of paste, ACI Proc. 43 (9) (1946) 469–504.
[26] D.E.-M. Bouhjiti, J. Baroth, M. Briffaut, F. Dufour, B. Masson, Statistical modeling of cracking in large concrete structures under Thermo-Hydro-Mechanical loads: Application to Nuclear containment buildings. Part 1: Random Fields Effects (reference analysis), Nuclear Engineering and Design 333 (2018) 196–223, https://doi.org/10.1016/j.nucengdes.2018.04.005.
[27] D.E.-M. Bouhjiti, M. Boucher, M. Briffaut, F. Dufour, J. Baroth, B. Masson, Accounting for realistic Thermo-Hydro-Mechanical boundary conditions whilst modeling the ageing of concrete in nuclear containment buildings: model validation and sensitivity analysis, Eng. Struct. 166 (2018) 314–338, https://doi.org/10.1016/j.engstruct.2018.03.015.
[28] M. Thiery, V. Baroghel-Bouny, N. Bourneton, G. Villain, C. Stefani, Modélisation du séchage des bétons. Analyse des différents modes de transfert hydrique, Revue européenne de Génie Civil 11 (2007) 541–577.
[29] Z.P. Bažant, L.J. Najjar, Drying of concrete as a non-linear diffusion problem, Cem. Concr. Res. 1 (5) (1971) 461–473.
[30] D. Gawin, F. Pesavento, B.A. Schrefler, Hygro-thermo-chemo-mechanical modelling of concrete at early ages and beyond. Part I: hydration and hygro-thermal phenomena, Int. J. Numer. Methods Eng. 67 (3) (2006) 299–331, https://doi.org/10.1002/nme.1615.
[31] J.H. Chung, G.R. Consolazio, Numerical modeling of transport phenomena in reinforced concrete exposed to elevated temperatures, Cem. Concr. Res. 35 (3) (2005) 597–608, https://doi.org/10.1016/j.cemconres.2004.05.037. URL: http://www.sciencedirect.com/science/article/pii/S000888460400239X.

[32] R. Mensi, P. Acker, A. Attolou, Séchage du béton: analyse et modélisation, Mater. Struct. 21 (3) (1988) 3–12, https://doi.org/10.1007/BF02472523.
[33] M.T. van Genuchten, A closed-form equation for predicting the hydraulic conductivity of unsaturated soils, Soil Sci. Soc. Am. 44 (1980) 892–898.
[34] R. Millington, Gas diffusion in porous media, Science 130 (1959) 100–102.
[35] K. Norling-Mjörnell, Moisture Conditions in High Performance Concrete: Mathematical Modelling and Measurements Ph.D. thesis, Chalmers University of Technology, 1997.
[36] M. Jirásek, Z.P. Bažant, Inelastic Analysis of Structures, John Wiley & Sons Ltd, 2002.
[37] S.-J.H.H.-G. Kwak, J.-K. Kim, Non-structural cracking in rc walls: Part i. finite element formulation, Cem. Concr. Res. 36 (4) (2006) 749–760, https://doi.org/10.1016/j.cemconres.2005.12.001.
[38] D. Gawin, F. Pesavento, B.A. Schrefler, Modelling creep and shrinkage of concrete by means of effective stresses, Mater. Struct. 40 (6) (2007) 579–591, https://doi.org/10.1617/s11527-006-9165-1.
[39] Z.P. Bažant, Y. Xi, Drying creep of concrete: constituve model and new experiments separating its mechanics, Mater. Struct. 27 (1) (1994) 3–14, https://doi.org/10.1007/BF02472815.
[40] F.H. Wittmann, P. Roelfstra, Total deformation of loaded drying creep, Concr. Res. 10 (5) (1980) 601–610, https://doi.org/10.1016/0008-8846(80)90023-X.
[41] K. Calonius, T. Nilsson, O. Elisson, S. Lehmann, EDF VERCORS Project: Benchmark 1: Themes 1, 2 and 3, Research Report, VTT Technical Research Centre of Finland, Finland, 2016, project code: 102783..
[42] Z.P. Bažant, Mathematical modeling of creep and shrinkage of concrete, John Wiley & Sons Inc, Chichester, 1988.
[43] Fédération Internationale du Béton, fib Model Code for Concrete Structures 2010, fib Bulletin, International Federation for Structural Concrete (fib), 2013..
[44] M. Jirásek, P. Havlásek, Microprestress-solidification theory of concrete creep: Reformulation and improvement, Cem. Concr. Res. 60 (2014) 51–62, https://doi.org/10.1016/j.cemconres.2014.03.008. URL: http://www.sciencedirect.com/science/article/pii/S0008884614000702.
[45] Z. Bažant, P. Havlásek, M. Jirásek, Microprestress-solidification theory: Modeling of size effect on drying creep, in: N. Bicanic, H. Mang, G. Meschke, R. de Borst (Eds.), Computational Modelling of Concrete Structures, CRC Press/Balkema, EH Leiden, The Netherlands, 2014, pp. 749–758.
[46] L. Granger, Comportement différée du béton dans les enceintes de centrale nucléaire: analyse et modélisation, Ph.D. thesis, ENPC (1995)..
[47] CEB, Evaluation of the time behaviour of concrete, report, CEB Group n9 (1990)..
[48] A. Foucault, S. Michel-Ponnelle, E. Galenne, A new crep model for NPP containment behaviour prediction, International Conference on Numerical modeling Strategies for Sustainable Concrete Structures (SSCS), Aix-en-Provence, France..
[49] G. De Schutter, Degree of hydration based kelvin model for the basic creep of early age concrete, Mater. Struct. 30 (4) (1999) 260–265, https://doi.org/10.1007/BF02479595.
[50] L. Charpin, Y. Le Pape, B. Masson, EDF study of 10-year concrete creep under uni axial and bi axial loading: evolution of Poisson coefficient under sealed and unsealed conditions, in: Proceedings of CONCREEP'10, Vienna, 2015, pp. 1381–1390.
[51] A. Hilaire, F. Benboudjema, A. Darquennes, Y. Berthaud, G. Nahas, Modeling basic creep in concrete at early-age under compressive and tensile loading, Nucl. Eng. Des. 269 (2014) 222–230.
[52] R. de Borst, Smeared cracking, plasticity, creep, and thermal loading – A unified approach, Comput. Methods Appl. Mech. Eng. 62 (1) (1987) 89–110, https://doi.org/10.1016/0045-7825(87)90091-0.
[53] Z.P. Bažant, B.H. Oh, Crack band theory for fracture of concrete, Mater. Struct. 16 (3) (1983) 155–177.
[54] M. Azenha, C. Sousa, R. Faria, A. Neves, Thermo-hygro-mechanical modelling of self-induced stresses during the service life of RC structures, Eng. Struct. 33 (12) (2011) 3442–3453.
[55] M. Azenha, L. Leitão, J.L. Granja, C. de Sousa, R. Faria, J.A. Barros, Experimental validation of a framework for hygro-mechanical simulation of self-induced stresses in concrete, Cem. Concr. Compos. 80 (2017) 41–54.
[56] A. Sellier, A. Millard, Weakest link and localization WL2: a method to conciliate probabilistic and energetic scale effects in numerical models, Eur. J. Environ Civ. Eng (18(10), 2014,) 1177–1191, https://doi.org/10.1080/19648189.2014.906368.
[57] J. Torrenti, V. Nguyen, H. Colina, F.L. Maou, F. Benboudjema, F. Deleruyelle, Coupling between leaching and creep of concrete, Cem. Concr. Res. 38 (6) (2008) 816–821, https://doi.org/10.1016/j.cemconres.2008.01.012.
[58] J. Mazars, F. Hamon, S. Grange, A new 3D damage model for concrete under monotonic, cyclic and dynamic loadings, Mater. Struct. 48 (11) (2015) 3779–3793, https://doi.org/10.1617/s11527-014-0439-8.
[59] J. Mazars, A description of micro and macroscale damage of concrete structures, Eng. Fract. Mech. 25 (1986) 729–737.
[60] F. Benboudjema, J.-M. Torrenti, Early age behaviour of concrete nuclear containments, Nucl. Eng. Des. 238 (2008) 2495–2506.
[61] G. Matheron, The intrinsic random functions and their applications, Adv. Appl. Prob. 5 (3) (1973) 439–468.